Digital in-line holography for large-volume analysis of vertical motion of micro-scale marine plankton and other particles

Zonghua Liu [1], Tomoko Takahashi [2], Dhugal Lindsay [2], Thangavel Thevar [3], Mehul Sangekar [1,2], Hiromi Kayama Watanabe [2], Nicholas Burns [3], John Watson [3], Blair Thornton [1,4]

1 *Institute of Industrial Science, University of Tokyo, Tokyo, Japan*; 2 *X-STAR, JAMSTEC, Yokosuka, Kanagawa, Japan*; 3 *School of Engineering, University of Aberdeen, Aberdeen, UK*; 4 *Centre for In Situ and Remote Intelligence, Faculty of Engineering and Physical Sciences, University of Southampton, Southampton, UK*

Abstract: Measuring the distribution, characteristics and dynamics of marine micro-scale plankton and other particulate matter is essential to understand the vertical flux of elements in the marine environment. Digital holographic microscopy is a powerful approach for measuring these and studying their 3D trajectories in a relatively large observation volume. This paper demonstrates a compact, in-line digital holographic microscope that allows large-volume and high-resolution recording of marine particles through combining a continuous wave laser and a short exposure CMOS camera with efficient global shutters. A resolution of better than 10 μm is demonstrated in air and the minimum distinguishable size of targets recorded in water is approximately 20 μm. The maximum volumetric throughput of the setup is 1904 mL/s. The microscope can take motion blur free holograms of particles moving at up to 490 mm/s in theory, and has been tested in the ~200 mm/s flowing water. The orientation of the measured volume improves the ability of digital holography in profiling sinking rates and active vertical migration. The system was tested onboard a research vessel to record a range of live plankton and other particles. The motion of some samples, including the sinking motion and swimming motion, was analysed using custom developed image processing software. The experimental results show that the combination of high resolution and a large volume over which motion of sparse-distribution particles can be tracked, can improve the ability to differentiate between different types of marine particle and identify behaviours of live plankton.

30 **Key words:** digital in-line holographic microscopy, large-volume recording, marine plankton and

31 particle motion tracking, vertical profiling of particulates, holographic image processing

32

1 Introduction

34 Micro-scale marine plankton and other particles play a key role in the vertical transport of carbon,

35 nitrogen, phosphorus, oxygen and other elements in the ocean. Their occurrence, variety and

36 distribution are indicators of marine ecosystem health and function [1],[2]. Active particles, such as

37 live plankton, use energy available in the environment to drive and trigger different motion patterns.

38 Monitoring these behaviours is important to understand their ecological and evolutionary strategies

39 [3],[4]. Global scale analysis of movements of marine particles is also vital to model the transport of

40 carbon and energy between organisms living near the surface and the deep sea. Examples of trends in

41 vertical matter transport [5] that need to be understood include ingestion, fragmentation and sinking

42 of faecal and other material [6],[7], as well as behaviours such as predation [8], escape [9] and

43 swimming [10]. However, due to the technical difficulty of monitoring the sparse distribution of

44 particles in the deep sea, the majority of such research has been focused on the upper ocean (shallower

45 than 200 m) and our understanding of these processes in the deep sea is limited [5],[6].

46

47 The traditional way to study micro-scale particles in the deep ocean is to recover samples using fine-

48 meshed nets and filters, and use an objective microscope to observe and analyse them in a laboratory.

49 However, reliance on ships to deploy equipment and offline analysis after the recovering of sampling

50 devices (*e.g.* microscopes) limit the spatial and temporal resolution and extent of monitoring possible,

51 due to the high cost and limited availability of crewed research vessels. Methods (*e.g.* Benthic

52 Underwater Microscope [11]) for *in situ* observations also exist. However, the narrow depth of field

53 makes standard objective microscopes unsuitable when large-volume observation is necessary, as

54　particle abundances are several orders-of-magnitude lower in the deep open ocean than in shallow

55　areas, making their distribution sparse and much harder to detect [5].

56

57　Optical imaging techniques such as shadowgraph [12] and fluorography [13], on the other hand, allow

58　large numbers of particles to be visualised in real time. These approaches are useful for analysing

59　particles in bulk, but they lack the ability to measure their 3D movement. However, to understand

60　ecological functions and their mechanisms, it is important to track the motion of particles with

61　sufficient resolution, and this is also helpful to identify what type of particles they are [7]. Holographic

62　imaging benefits from a much longer field depth relative to image resolution than other optical

63　techniques [14],[15]. Digital holographic microscopy (DHM) has been used to study the 3D motion of

64　marine particles and organisms [8]-[10],[16],[17], investigating response to controlled stimuli of

65　targets that have been physically constrained in laboratory conditions. To study the distribution of

66　unconstrained plankton and other particles, ocean deployable *in situ* holographic microscopes such as

67　Holosub [18], [19], eHoloCam [20], HoloSea [21] and LISST-Holo2 [22] have been developed (see

68　TABLE 2). However, large volumetric throughput (*e.g.* Holosub and eHoloCam) holographic devices

69　for studying deep-sea particles typically use pulsed lasers that are large and power-hungry, which

70　makes them unsuitable for long-term recording in deep water.

71

72　The aim of this paper is to investigate a method to track the 3D motion of micro-scale particles at a

73　resolution high-enough (~20 µm) to identify their type from their morphology, and over a volume that

74　is large enough (~12 mL) to identify sparsely distributed particles and gather reliable measurements

75　of their vertical motion. To achieve this, we demonstrate the combination of a continuous wave (CW)

76　laser and a fast CMOS sensor with low parasitic gain to achieve high resolution and motion blur free

77　holograms of marine particles. This compact, low power instrument can achieve up to 1904 mL/s

78　volumetric throughput, which is on the scale needed for monitoring of deep-sea particulate matter. The

79   method is demonstrated using an experimental setup to measure the vertical/3D motion of living/non-

80   living particles in seawater.

81

2 Measurement System

83   A lensless, in-line DHM is developed with the capability of recording micrometre-order spatial

84   features of marine particles, such as micro- and meso- plankton (20 – 2000 µm [23]). A CW laser is

85   used as the light source. An alternative is to use pulsed lasers to capture motion blur free images of

86   moving objects. However, pulsed lasers are typically more expensive, larger and less robust to failure

87   than conventional CW lasers due to the larger number of photoelectric components and increased risk

88   of optical damage. In order to achieve motion blur free images using a CW laser, we use a CMOS

89   camera with a short exposure time. While the microsecond-order exposure time achieved by using

90   CMOS cameras is still several orders of magnitude longer than a nanosecond pulsed laser, it is not an

91   issue to record motion blur free images using a sensor with a ~5 µm resolution and ~10 µs exposure

92   time when imaging targets that laterally move with a relative speed of less than 500 mm/s (5 µm / 10

93   µs). The 10 µs exposure is low enough to record active marine particles, such as plankton, with mean

94   *in situ* swimming speeds ranging from about 10 to 90 mm/s [24] (see TABLE 1 for some species). The

95   efficient global shutter [25] with a low parasitic light sensitivity in the camera also facilitates capturing

96   the shape of fast-moving targets.

97

98

99

100

101

102

103   TABLE 1. MOTION SPEEDS OF SOME MARINE PLANKTON

Marine Plankton	Average Motion Speed (mm/s)
Acartia tonsa nauplii [9]	escape swimming: 15.0 − 29.5
Temora longicornis adults [26]	swimming: 2 − 10
Temora longicornis nauplii [27]	swimming: 0.03 − 1.23
Heterosigma akashiwo [28]	swimming: ~0.5
Prorocentrum minimum [10]	swimming: ~0.1

104

105   In order to improve the functionality of DHM for measuring a large range of motion in the vertical

106   direction, the measurement channel is designed to be upright and the system appearance looks like a

107   real microscope. Another reason for this design is that the system is expected to be mounted on some

108   ocean platforms in the future, such as Argo floats and gliders. Considering mountable compatibility

109   with other devices, the system cannot be designed to be too long. Besides this, the high-resolution

110   recording requirement also restricts the body length of the system [15].

111

112   2.1 Optics Design

113   The optical components are arranged to make inline measurements of a vertically oriented channel as

114   illustrated in Fig. 1. The setup consists of two main housings: a flow tube and a waterproof hull. The

115   length of the measurement channel in the flow tube is 200 mm, with an internal diameter of 16 mm. A

116   compact 785 nm wavelength single mode CW laser (Oxxius LBX-785S-150-ISO-PPF, 40 × 40 × 100

117   mm) is used as the light source. Near infrared light was chosen because plankton tends to exhibit low

118   sensitivity to this wavelength [29],[30]. The laser is coupled to a single mode fibre (Thorlabs P3-

119   780AR-2), and light coming out of the fibre is collimated in a waterproof housing. This collimated 12

120   mm diameter beam passes through a sapphire window (Thorlabs WG31050) to illuminate particles

121   suspended in the measurement channel. The light passes through the second sapphire window

122   (Thorlabs WG31050) and an attenuation filter (OptoSigma AND-25C-20) before being recorded by a

123   CMOS detector (JAI GO-5100-USB, 29 × 29 × 41.5 mm). The detector has a resolution of 2464 ×

124   2056 with a pixel pitch of 3.45 × 3.45 μm (Binning 1 mode), giving an active area of 8.5 mm × 7.09

125   mm. The volume observed in each frame using this setup is 12 mL (8.5 mm × 7.09 mm × 200 mm),

126   where the maximum frame rate at the 3.45 μm resolution is 74 fps, giving a theoretical maximum

127   volumetric throughput of 892 mL/s. It can work in another mode (Binning 2) where a square of four

128   adjacent pixels is binned as one pixel. In this mode, the pixel pitch becomes 6.90 μm × 6.90 μm, and

129   the frame rate can reach 158 fps, which improves the maximum volumetric throughput to 1904 mL/s.

130   The flow through the tube can be controlled by connecting a pump at the outlet valve.

131

132   The detector has a short exposure time of 7 μs with low parasitic exposure (< 0.002%) when the

133   electronic shutter is closed, allowing high-resolution motion blur free capture of objects moving at up

134   to 490 mm/s (3.45 μm / 7 μs, please see details in Section 3.2) in theory, which is sufficient to record

135   the 3D motion of many active marine particles. This movement tolerance will also enable the proposed

136   system to be mounted on Argo floats and gliders (Argo floats – ~100 mm/s, gliders – ~350 mm/s) in

137   future.

138
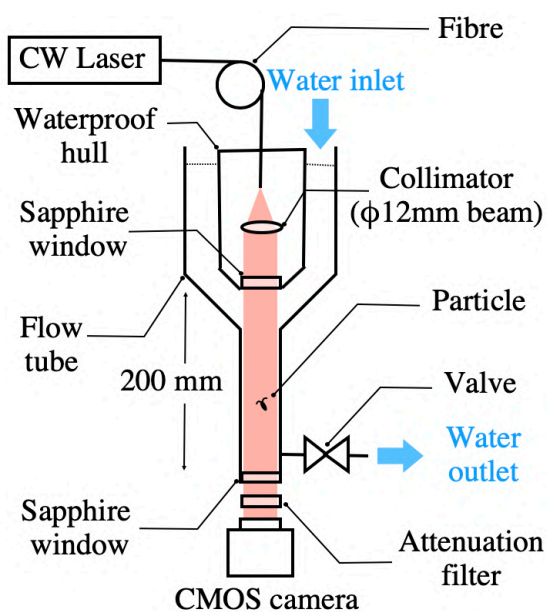
139
140   Fig. 1. Schematic of the in-line holographic microscope.
141

142   TABLE 2 shows the specification of six representative holographic imaging systems and the system

143   developed in this work. The nanosecond pulsed lasers adopted in Holosub, eHoloCam and HoloSea

144   allow measurements of particles that move several orders of magnitude faster than CW laser systems.

145   However, this is significantly faster than the speed of the particles targeted in this work. Like Holosub

146   and eHoloCam, the large volumetric throughput makes the proposed setup more suitable for measuring

147   sparsely distributed plankton and particles than other instruments which also use a CW laser.

148

149   TABLE 2. SPECIFICATIONS OF SIX REPRESENTATIVE SYSTEMS AND THAT DEVELOPED
150   IN THIS PAPER

System	Size (diameter × length: mm²)	Laser Mode	Minimum Pixel Pitch (µm)	Maximum Movement Tolerance * (mm/s)	Maximum Frame Rate (fps)	Sampling Volume Per Hologram (mL)	Maximum Volumetric Throughput (mL/s)
Holosub [18]	/ **	pulsed (50 ns)	7.4	1.48×10^5	14.7	40.5	595
eHoloCam [20]	330 × 1350	pulsed (5 ns)	3.5	7×10^5	25 ***	36.5	~920
HoloSea [21]	92 × 351	pulsed (500 ns)	~2.0	$~4.1 \times 10^3$	22	~0.3	~6.6
LISST-Holo2 [22]	133 × 767	continuous	4.4	/	25	~2	45.6
Submersible Holographic Particle Imager [31]	~100 × 630	continuous	7.4	740	25	~1.7	~42.5
DIHM in [32]	~150 × 890	continuous	7.4	118	7	1.8	12.6
Our System	~158 × 502	continuous	3.45	490	158 ****	12	1904

151   * This specification is calculated by dividing the shortest exposure time by the minimum pixel pitch.
152   ** / indicates there is no information found about this specification.
153   *** at pixel pitch of 10.5 µm
154   **** at pixel pitch of 6.90 µm
155

2.2 Data Processing

157   The data processing in this work extracts the 3D position of particles in the imaging volume from

158   reconstructed holograms. The angular spectrum method [33] is used to reconstruct holograms in this

159   study. The depth positional information of an object is obtained using the focus metric of absolute

160   Tenengrad [34], shown in Eq. (1):

161

162    $T_{grad} = \sum_{i,j}(|f(i,j) \otimes S| + |f(i,j) \otimes S'|), (1)$

163

164   where $f(i,j)$ signifies an image and $\otimes$ indicates convolution; S and S' are the two Sobel kernels with

165    $S = [1\ 0 - 1;\ 2\ 0 - 2;\ 1\ 0 - 1]$. In order to improve its performance, a weight is given to each

166   gradient value by multiplying the edges detected using structured forests [35]. Eq. (1) now becomes:

167

168    $T_{grad} = \sum_{i,j}(|f(i,j) \otimes S| + |f(i,j) \otimes S'|) \cdot e(i,j), (2)$

169

170   where, $e(i,j)$ is the edge image.

171

172   Fig. 2 shows the focusing performance of the two metrics on two holograms. These two images show

173   that the weighted absolute Tenengrad outperforms the normal Tenengrad when they are used to

174   automatically look for the focused reconstructing distance for a hologram. Each hologram is processed

175   with 1000 reconstructing slices at 0.2 mm range intervals.

176

177
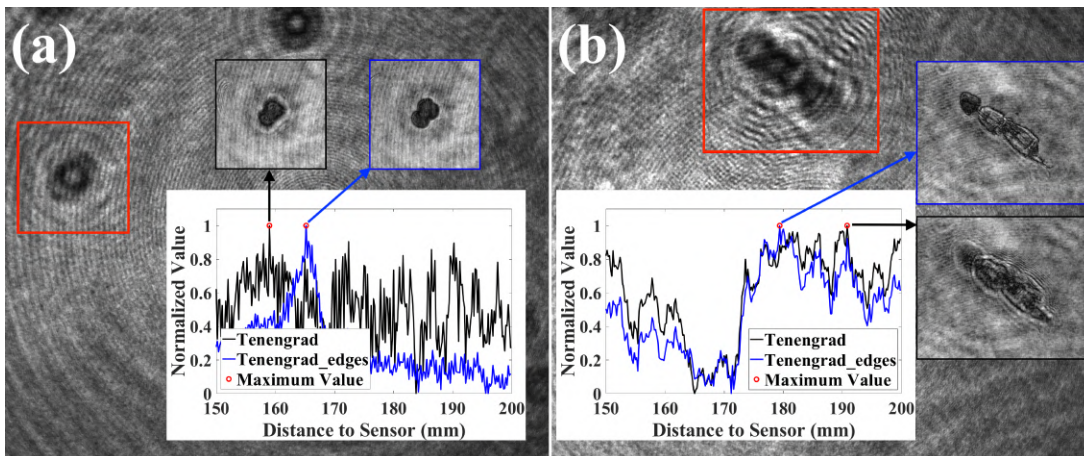
Fig. 2. Performance of two focus metrics on two holograms. The plotting figures show the Tenengrad values (normalised in the range from 0 to 1) of the outlined regions (in the red boxes) that are calculated in a distance range from 150 mm to 200 mm. The focused reconstructions of the region based on the two metrics are also displayed on each hologram.

To determine the (x, y) plane position of the target in the focused reconstruction, the target particle is

segmented using a convex hull tool that is constrained by manually identified dominant points on its

outline (see Fig. 3). The centroid of the segment is calculated and converted from the image frame to

the spatial frame. Combining this with the focus distance gives the 3D coordinate of the centre of each
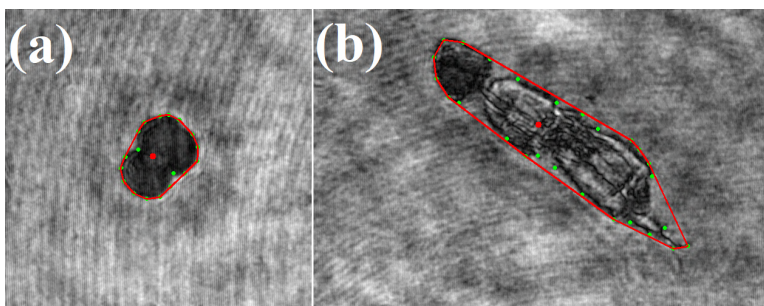
object.

Fig. 3. Two examples showing the drawn convex hull (red line) based on the selected dominant points (green points) and object centres (red point) whose 3D coordinates are (298, 766, 165.2) and (1056, 290, 179.4) respectively. These two images are cropped from their focused reconstructions after auto-focusing. The (x, y) position is calculated based on the full image dimension.

3 System Performance Analysis

3.1 Resolution Estimation

Resolution in DHM depends on some parameters of the setup [16], such as the laser wavelength, and the size and recording position of the sensor. It includes the lateral resolution (in the x-y plane) and longitudinal resolution (along z direction). The resolution of a digital holographic camera can be estimated theoretically and experimentally. The calculation of resolution in theory is normally based on the Rayleigh and Sparrow criteria [36], and the experimental estimation is usually implemented using a resolution target.

3.1.1 Longitudinal Resolution and Reconstructing Interval

The longitudinal resolution can be defined as the minimum distance between two discrete point targets along the optical axis that can be resolved in the recorded image. This resolution in DHM is difficult to directly measure, especially in the in-line setup [16]. However, it is necessary to know this parameter because it determines the minimum interval in direction z during reconstructing a hologram. It is suggested that this resolution can be indirectly estimated through computing the quality of reconstructions at different reconstructing distances [37].

Eq. (2) is used during indirectly estimating the longitudinal resolution of the instrument in this work. The procedure is: for a hologram, first use Eq. (2) to compute T_{grad} of its focused reconstruction at distance d_{focus} (this focused reconstruction is obtained from the auto-focusing algorithm described in Section 2.2); and this equation is also used to compute T_{grad} in a reconstruction reconstructed at a given distance d; the difference of these two reconstructions is then computed based on the equation below.

224     $Difference\ (d) = \frac{|T_{grad}(d) - T_{grad}(d_{focus})|}{T_{grad}(d_{focus})}.$ (3)

225

226   This equation above is used to calculate the difference between the focused reconstruction and out-of-

227   focus reconstructions of the regions of interest in the two holograms in Fig. 2. Their focused

228   reconstructions are shown in Fig. 3. For the region in (a), its focus distance is 165.4 mm, and the

229   estimation distance range is from 155 mm to 175 mm; for region (b), its focus distance is 179.4 mm,

230   and the estimation distance range is from 170 mm to 190 mm. The reconstructing interval is 0.01 mm.

231

232   Fig. 4 shows the results from the two regions. Since much noise exits, two curves fluctuate sharply.

233   However, it can still be observed that the values quickly decrease beside the focuses in the two curves.

234   This indicates that unfocused reconstructions reconstructed at distances close to the focus become

235   significantly similar with the focused reconstruction ($< \sim 5\%$ in difference) and they become

236   undistinguishable. Therefore, if the threshold of difference is set as 5%, the longitudinal resolution of

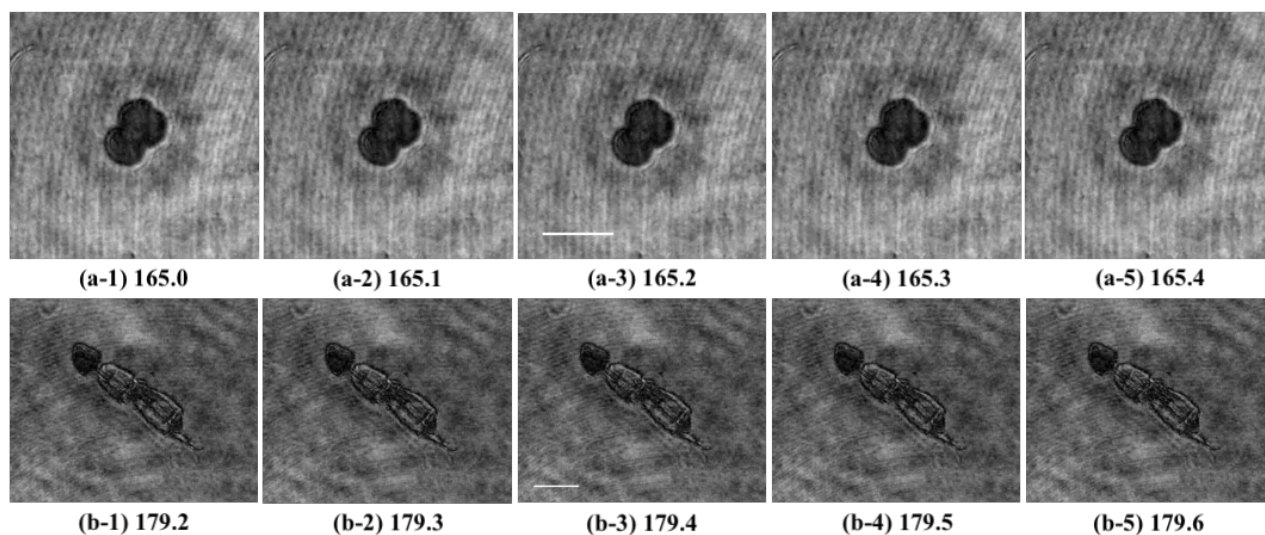237   the setup can be speculated to be around 0.2 mm based on the measure of Eq. (3).

238
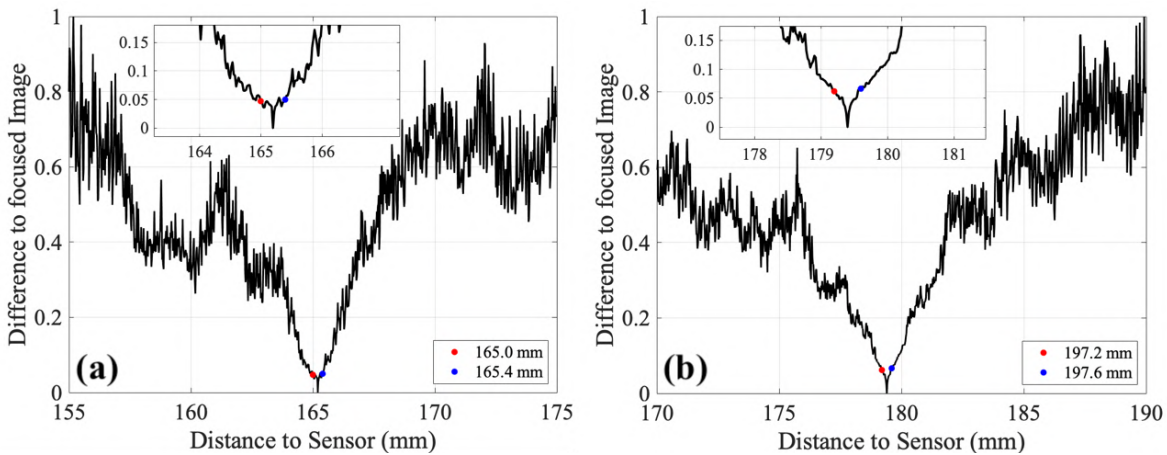
239
240 Fig. 4. Two examples showing the difference between the focused image and unfocused images. (a)
241 shows the difference values calculated on region (a) in Fig. 3, and (b) shows the values on region (b)
242 in Fig. 3. The magnified figures show the detail of the peaks. The peaks are located at their focus
243 distances respectively (165.2 mm and 179.4 mm). The red and blue spots are localised at -0.2 mm and
244 +0.2 mm from the focus respectively.
245

246   Theoretically, it should be better if the reconstructing interval is defined as smaller as possible.

247   However, that will make the reconstructing procedure too time-intensive. The reconstructing interval

248   in practice should be decided by the longitudinal resolution. Since the exact longitudinal resolution of

249   DHM is difficult to achieve, the interval can be decided by the speculated value based on the given

250   measure and it is defined as 0.2 mm in this paper.

251

252   Another factor that affects the reconstructing interval is the target size, and the interval should be

253   smaller when reconstructing holograms of smaller targets. The sizes of the main objects observed in

254   this paper are in the range of several hundreds of micrometres to several millimetres. Fig. 5 shows

255   several reconstructions of the two regions in Fig. 3 around their focus distances. The sizes of the objects

256   are around 500 μm (in the top row) and 2 mm (in the bottom row). For each object, it can be observed

257   that reconstructions of within 0.2 mm from its focus are visually same with the focused reconstruction

258   ((a-3) and (b-3) respectively). Therefore, the reconstructing interval of 0.2 mm is reliable during

259   reconstructing holograms in this work.

(a-1) 165.0   (a-2) 165.1   (a-3) 165.2   (a-4) 165.3   (a-5) 165.4

(b-1) 179.2   (b-2) 179.3   (b-3) 179.4   (b-4) 179.5   (b-5) 179.6

260

261   Fig. 5. Reconstructions of two regions in Fig. 3 at several different distances. Their focus distances are
262   165.2 mm (a-3) and 179.4 mm (b-3) respectively. The scales indicate 500 μm in (a-3) and (b-3).
263

264

265

266   3.1.2 Lateral Resolution

267   *In air:* The theoretical lateral resolution of a reconstructed in-line hologram in air, r, can be

268   approximately calculated using Eq. (4) [15], [16]:

269

270    $r = \frac{\lambda}{D} d$, (4)

271

272   where λ is the laser wavelength, D is the diameter of the holographic image (normally simplified to

273   the image diagonal length), and d indicates the distance of the image plane to the sensor plane. The

274   resolution that is achieved is dependent on the distance of the image plane from the sensor plane due

275   to the diffraction limit as shown in Fig. 6 (black line). The actual lateral resolution can be measured

276   using a resolution target. Fig. 6 shows the experimentally derived lateral resolution of our setup that

277   was measured using a resolution target (ThorLabs NBS1963A) in air. Measurements were carried out

278   for an image plane distance of 70 to 270 mm at an interval of 20 mm.

279

280   The pixel pitch of the detector also limits the achievable resolution. This is shown in Fig. 6, where the

281   resolution of the nominal 3.45 μm pixel pitch of our detector is shown in red (Binning 1), and the

282   resolution for double binning (Binning 2), where 4 pixels are binned together with an effective pitch

283   of 6.90 μm shown in blue. Beyond 180 mm range, the two modes are almost identical since the lateral

284   resolution is diffraction limited. However, when the image plane is closer than 180 mm the smaller

285   pixel pitch in the nominal mode has a higher resolution, achieving a maximum of 8.8 μm at 70 mm

286   range.

287
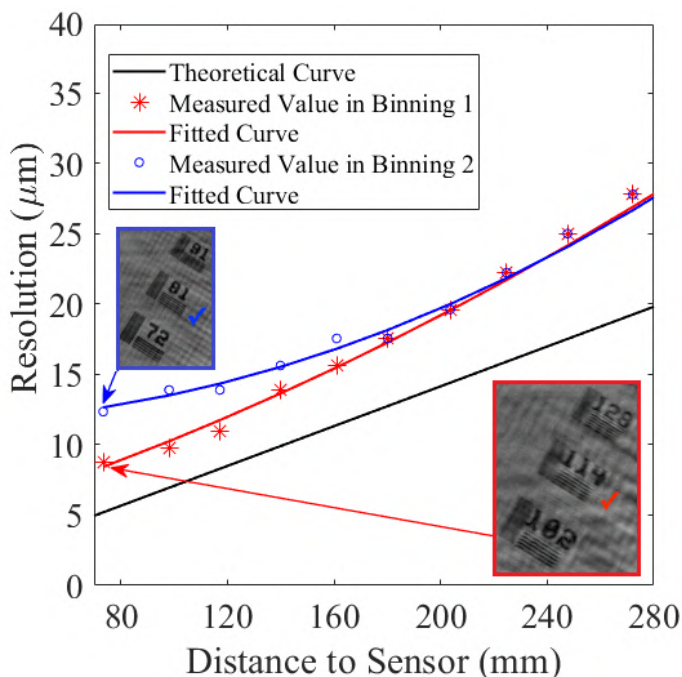
288
289 Fig. 6. Lateral resolution of the system in theory (black line) and measured experimentally. The
290 experiment for the pixel pitch of 3.45 μm (Binning 1) is in red, and Binning 2, which has an effective
291 pixel pitch of 6.9 μm is shown in blue. The two images show the best resolution in the two modes,
292 where Binning 1 can resolve 114 lines per mm, and Binning 2 can resolve 81 lines per mm,
293 corresponding to lateral resolutions of 8.8 and 12.3 μm respectively (at 70 mm distance to sensor). The
294 fitted curves are generated using the method of polynomial curve fitting.
295

296 *In water:* Since the flow channel is narrow (16 mm diameter), it is difficult to place the resolution

297 target in the channel to measure the actual lateral resolution of the system in water. This parameter is

298 estimated by the size of the minimum visible particles recorded by the system. Fig. 7 shows two

299 particles at the scale of 20 μm recorded when the pixel pitch is 3.45 μm. Their basic shape features are

300 discernible. Therefore, we speculate that the system at best could be able to discriminate particles with

301 the scale of 20 μm at this resolution.

302
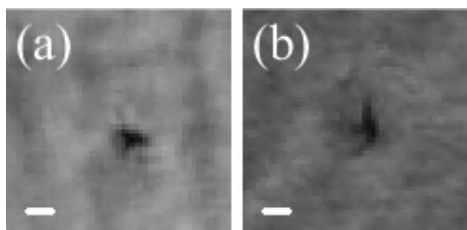
303
304 Fig. 7. Two particles recorded at the distance of 70 mm when the pixel pitch is 3.45 μm. The scales
305 indicate 20 μm.
306

307 3.2 Motion Blur Estimation

308 Motion blur is caused by target moving with respect to the camera during the period of exposure time.

309 It is determined by the object moving speed, and camera exposure time and viewpoint towards the

310 target [38]. A simple equation [39] used to calculate motion blur of a moving target is:

311

312 $Blur_{motion} = vt_e,$ (5)

313

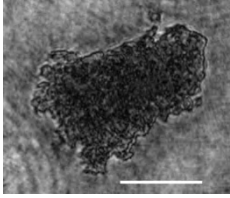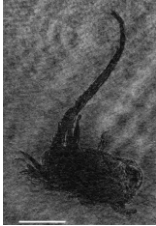314 where, v is the object moving speed and t_e is the camera exposure time.
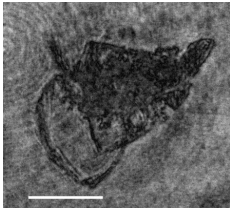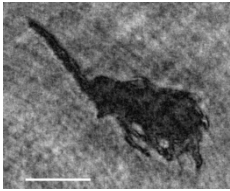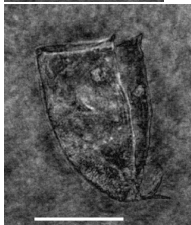
315

316 Theoretically speaking, if the motion blur projected to the sensor plane is less than a pixel length, this

317 blur cannot happen in a digital image. The camera pixel size in our system is 3.45×3.45 μm. Therefore,

318 based on Eq. (5), as long as the target moves at a speed less than 490 mm/s (3.45 μm / 7 μs), the camera

319 should be able to capture its moving without motion blur.

320 Since it is nearly impossible to exactly control the moving speed and direction of an object towards to

321 the sensor in water, it is difficult to provide an experimental test of the maximum movement speed.

322 However, we recorded many holograms of lifeless organic samples in flowing water with different

323 speeds (*e.g.* dead plankton, the active moving can be avoided using dead samples such that the flow

324 speeds can roughly be regarded as the moving speeds of the samples). The maximum flow speed tested

325 was around 200 mm/s. The exposure time of the camera was 7 μs and the pixel pitch size is $3.45 \times$

326 3.45 μm. Some examples are shown in TABLE 3. The reconstructed holograms recorded in flowing

327 water look similar with the reconstructed holograms recorded in the still water, and no motion blur can

328 visually be observed on them. This indirectly shows that the setup is able to record clear holograms of

329 moving particles with a speed of around 200 mm/s at least. This speed tolerance has actually been high

330 enough to record most of moving plankton in oceans.

331

332 TABLE 3. HOLOGRAMS RECORDED IN STILL WATER AND FLOWING WATER WITH
333 DIFFERENT SPEEDS

Flow Speed (mm/s)	Sample1	Sample2
0.0		
~ 153.9		
~ 175.2		
~ 196.4		

334 Note: The scales indicate 500 μm.
335

4 Experimental Results

337 Some experimental results are shown in this section. In the experiments below, the camera exposure

338 time was set as 7 μs and the frame rate was 10 fps. The beam intensity after the collimator was about

339 11 mW, and it became ~2 mW after the beam passed through the attenuation filter (transmissivity –

340 20%) when there was no water in the measurement chamber.

341

342 The image processing methods used to process holograms have been described in Section 2.2,

343 including the algorithms of auto-focusing and object position extraction.

4.1 Recording Marine Plankton

344

345   The measurement system was used to record and study plankton and other particles during a cruise of

346   the R/V *Yokosuka* (YK20-E02) conducted in February 2020 in Sagami Bay and Suruga Bay, Japan.

347   Fig. 8 shows some plankton recorded during the cruise. These were collected from a large range from

348   deep sea to upper ocean using a net mounted on a Deep Tow camera system [40] and observed onboard

349   the ship soon after being recovered on deck. The measured plankton included a copepod larvae in (a

350   and b), larvaceans in (c) and (f), a jelly in (d), a copepod nauplius larva in (e), a euphausiid furcilia

351   larva in (g), copepods in (h, i, j and k), and a chaetognath in (l). Their sizes range from a few hundred

352   microns (a, b) to several millimetres (k and l).

353
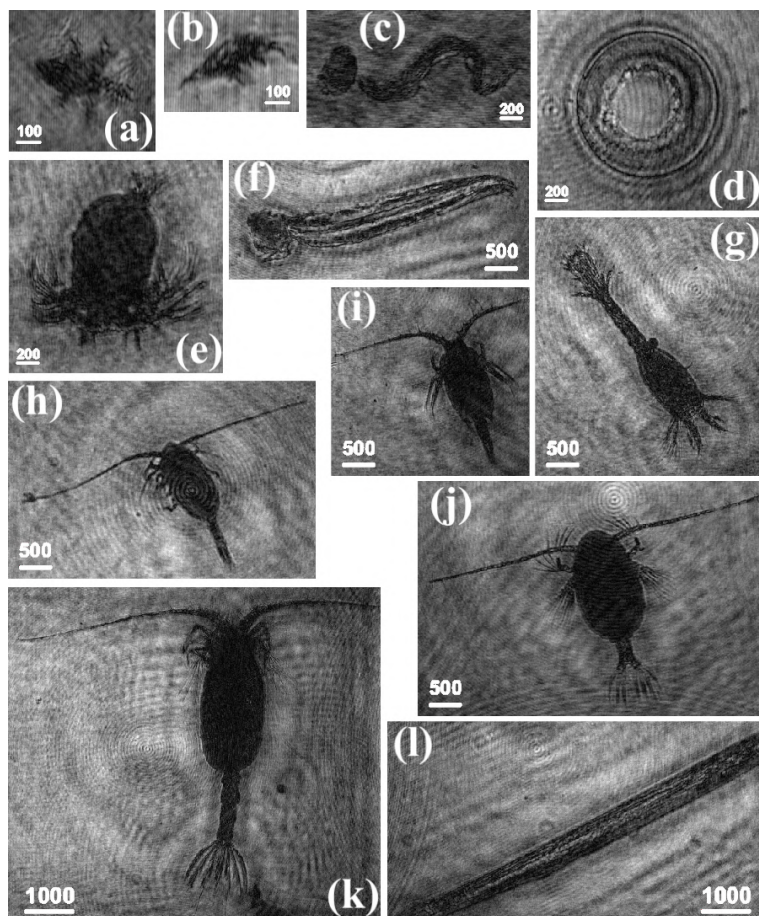
Fig. 8. Plankton recorded during the cruise. The unit of scale in the images is μm.

4.2 Tracking Trajectories of Marine Plankton and other Particles

358

359   4.2.1 Sinking Motion

360   The vertical motion of a trachymedusan jellyfish (see Fig. 9 (a)) was measured in sea water. The

361   holograms were reconstructed to obtain the distances to the sensor plane at different time points. Fig.

362   9 (b) shows one of the reconstructed holograms.

363
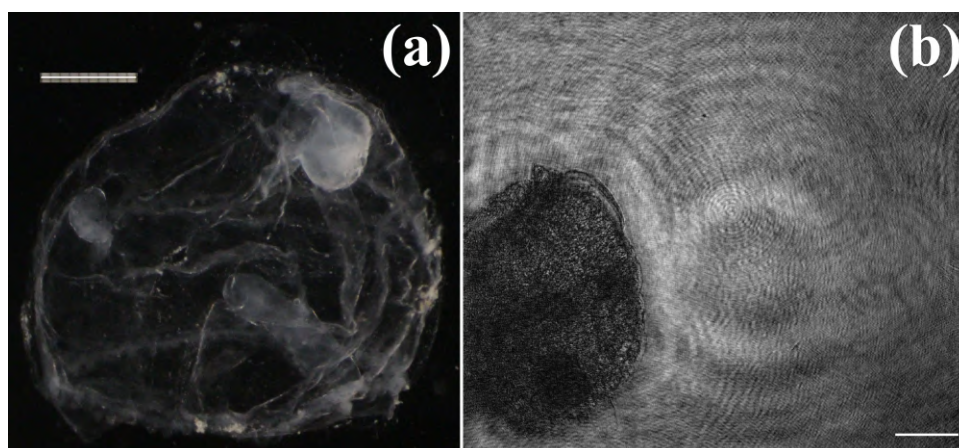
364
365   Fig. 9. Microscopic photograph of the jellyfish sample (a) and one of its reconstructed holograms (b).
366   The scales indicate 1000 µm.
367

368   Fig. 10 shows the distances and sinking speeds of the jelly over a 20 s period, where the speed is

369   determined by taking the derivative of the distance to the sensor. The sample sank from 256.0 mm to

370   168.2 mm in 20 s. The average sinking speed was 4.48 mm/s, with the particle accelerating downwards

371   at a rate of 0.04 mm/s^2 during this period.

372
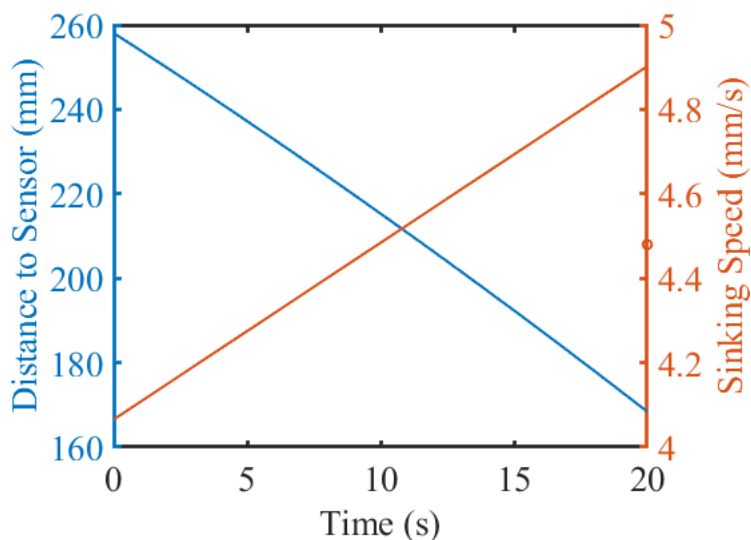
373
374 Fig. 10. Distances (blue) between the jelly sample and the sensor and its sinking speeds (brown) at
375 different time points. The open circle on the right y-axis indicates the average sinking speed. The
376 curves are fitted using the method of polynomial curve fitting.
377

378 We also measured the sinking speeds of some dried foraminifera particles (their main component is

379 $CaCO_3$) in water. Fig. 11 (a) shows a photograph of them and images (b)-(g) show the reconstructed

380 holograms of six of these particles. These six particle samples were recorded one by one. Unlike living

381 organisms, these inorganic particles cannot actively move at all. Their density is normally greater than

382 jellies and they tend to sink faster (see TABLE 4). The sinking speed has a relationship with the density

383 and volume. However, the motion of particles in water is a complex phenomenon and a detailed

384 description is not the focus of this paper. Fig. 12 depicts the sinking speeds of the six samples in the

385 distance range of 150 mm to 200 mm from the sensor and TABLE 4 lists the average speeds of them

386 during sinking. These data show that bigger particles tend to sink faster. It can also be observed that

387 the sinking speeds of these particles decreased with transit time, while the jelly's speed increased as

388 shown as in Fig. 10.

389
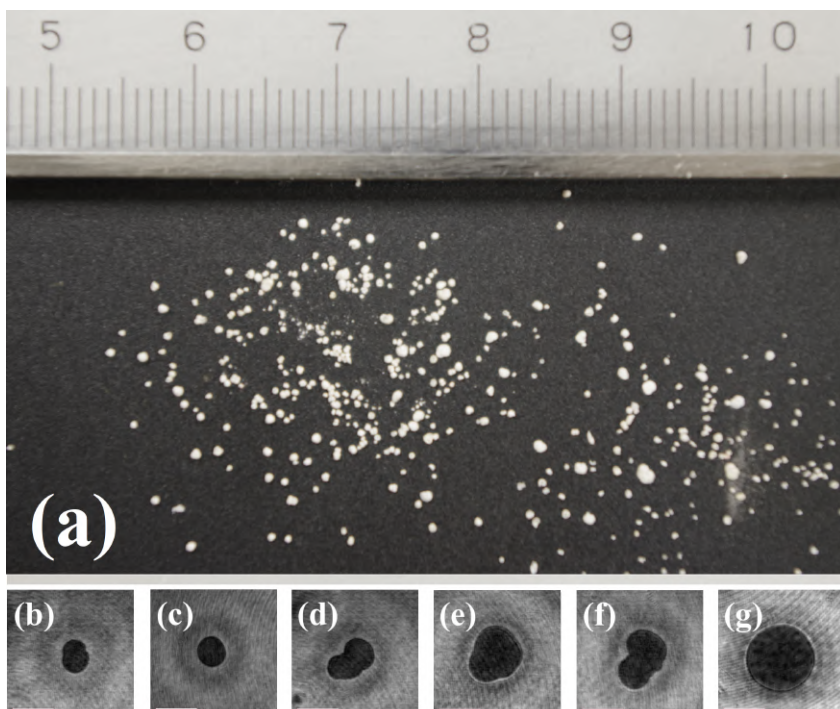
Fig. 11. Photograph of dried foraminifera particles (a) and reconstructed holographic images of six samples: (b) – Fora1; (c) – Fora2; (d) – Fora3; (e) – Fora4; (f) – Fora5; (g) – Fora6. The unit of the scale in (a) is mm. The scales in (b)-(g) indicate 500 μm.
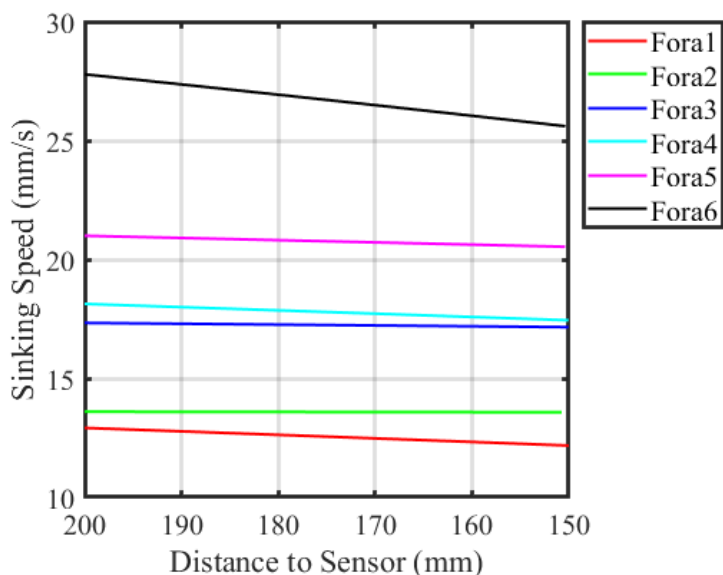
Fig. 12. Sinking speeds of six foraminifera particles at different distances to the sensor. The curves are generated using the method of polynomial curve fitting.

TABLE 4. AVERAGE SINKING SPEEDS OF THE JELLY AND SIX FORAMINIFERA PARTICLES

Sample	Jelly	Fora1	Fora2	Fora3	Fora4	Fora5	Fora6
Average Sinking Speed (mm/s)	4.48	12.55	13.59	17.24	17.79	20.76	26.66

402   4.2.2 Swimming Motion

403   The 3D swimming trajectory of a live calanoid copepod (as shown in Fig. 13 (a)) was measured in

404   seawater. Fig. 13 (b) and (c) are two reconstructed holograms of the sample. The (x, y) position of the

405   copepod in each image was determined as described in Section 2.2. Their body outlines and the centre

406   coordinates in 3D are shown in (b) and (c). It should be noted that the projected shape of the copepod

407   changes significantly during swimming behaviours and this limits the accuracy of the motion tracking

408   and velocity measurements made by the system.

409
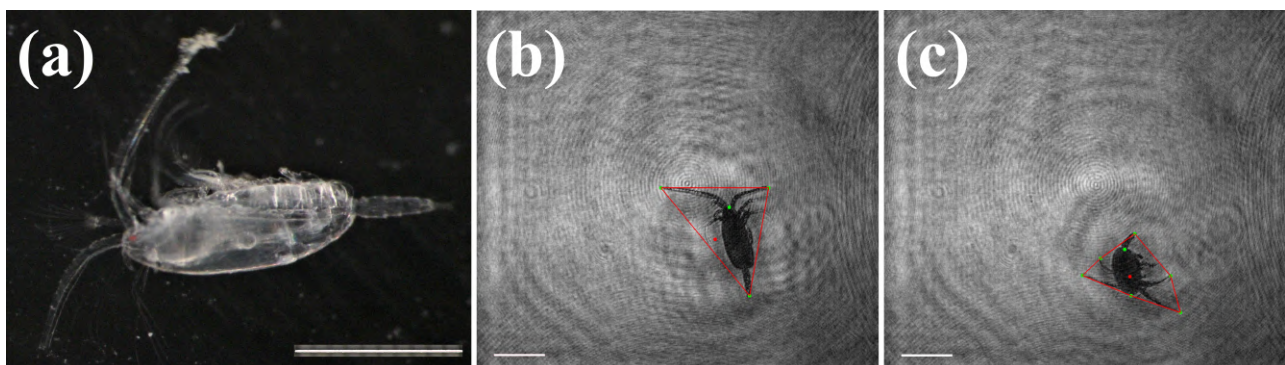
410
411   Fig. 13. Microscopic photograph of the copepod sample (a) and two reconstructed holograms (b) and
412   (c). The red convex hulls describe the body outline in the current moment and the red spots show its
413   3D coordinates that are (1360, 1301, 211.6) and (1402, 1512, 216.0) respectively. The (x, y) position
414   is calculated based on the sensor dimensions. The scales indicate 1000 μm.
415

416   Fig. 14 shows the 3D trajectory of the free-swimming copepod over 14 s. The red spots indicate the

417   copepod positions at intervals of 0.2 s, and the arrows indicate its swimming directions. The tracked

418   trajectory started at P1 (x = 3.91, y = 0.49, z = 231.0 mm) where the origin was measured at the top

419   left point of the CMOS detector. The red points initially stay close to each other, showing that the

420   copepod moved slowly laterally. The copepod then turned clockwise at 6 s (at P30) and accelerated

421   sharply between P33 and P34 reaching 18.97 mm/s. It then turned back and moved laterally again,

422   changing direction again at 9.2 s (P46). The winding trajectory with different colours describes that

423   the sample slowly sank, it swam up when sensing it had been sinking, and it would sink again. The

424   copepod gradually sank during the entire period on average, but propelled itself upwards at some points

425   in time. The total distance travelled was 63 mm in 14 s, with an average swimming speed of 4.50 mm/s.

426

427   Fig. 15 shows the reconstructed holograms of the copepod at five time points (P30, P33, P34, P35 and

428   P46 in Fig. 14). It can be observed that the copepod tended to turn its body over to change its swimming

429   direction, as shown in (a), (c) and (e). It kept its body flat and folded its legs when it moved in a high

430   speed, as shown in (b) and (d).

431
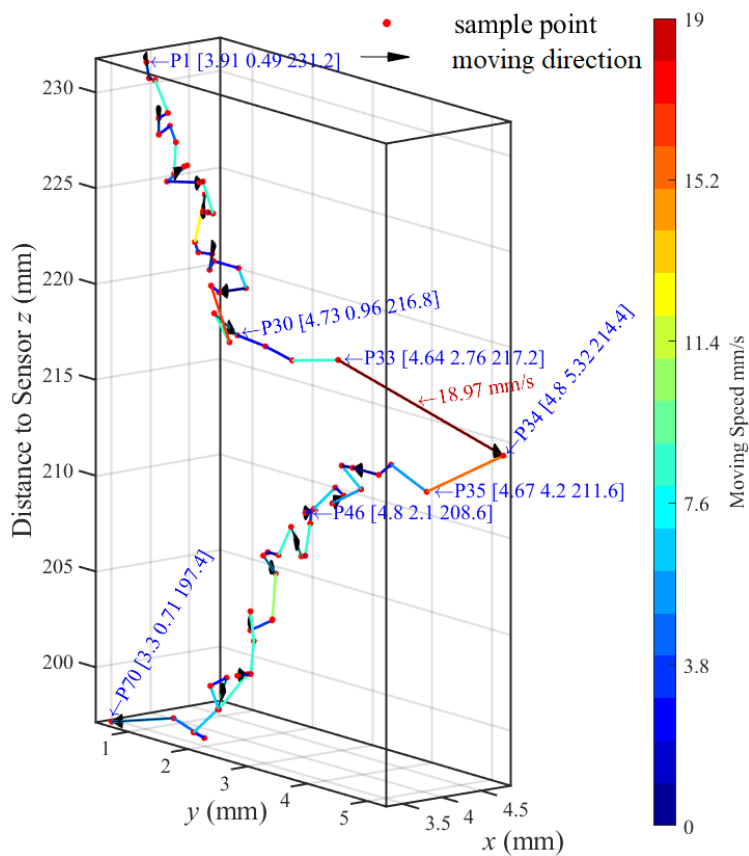
432
433   Fig. 14. 3D swimming motion of the copepod. The red dots correspond to its positions sampled every
434   0.2 s. The arrows indicate its swimming directions. The coordinates in blue show some sampling points.
435   The colormap describes the average speed between two sampled points.
436
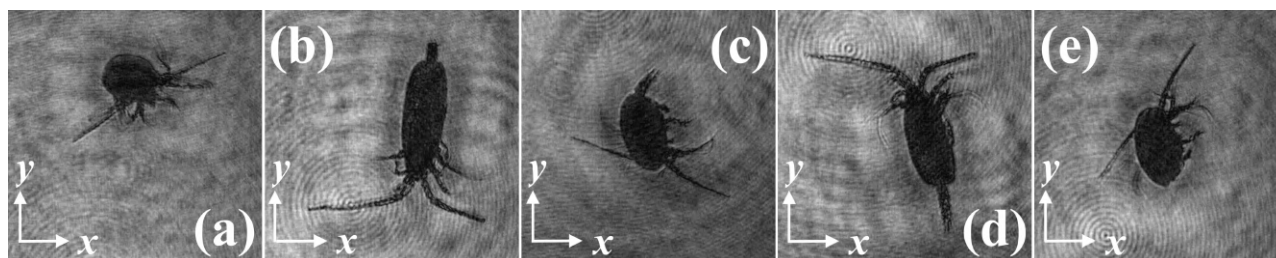
Fig. 15. Reconstructed holograms of the copepod at five time points. (a) – P30, (b) – P33, (c) – P34, (d) – P35, (e) – P46. The x and y axes have the same direction with the axes in Fig. 14.

4.2.2 Moving Speed *vs* Shape in Copepods

The high-resolution of the measurement system means that it is possible to resolve the shape of the copepod during different motion manoeuvres and investigate how the size of the target correlates with the swimming motion. The trajectories of six copepods with different sizes were tracked in Fig. 16, which shows their reconstructed holograms. The size of each copepod can be estimated from the reconstructed image.

Fig. 17 (a) shows their sinking speeds which reflect the typical motion of copepods where they slowly sink with fluctuating speeds. The vertical speed of the two smallest copepods, Cop1 and Cop2, fluctuated more widely along the z axis than the other targets. Big copepods tended to have high average sinking speeds (*e.g.* Cop5 and Cop6 in TABLE 5.) Generally speaking, copepods sink more slowly than smaller moribund jellyfish and foraminifera particles (see TABLE 4 and TABLE 5) owing to their active moving with the aid of antennae and legs. Images (b)-(g) show the moving trajectories and the instantaneous moving speeds of samples in the (x, y) plane. TABLE 5 also gives their average moving speeds in the (x, y) plane. The results show that the copepods moved freely in the horizontal plane (x-y plane) and they tended to have faster moving speeds in this plane than in the vertical direction (z axis).
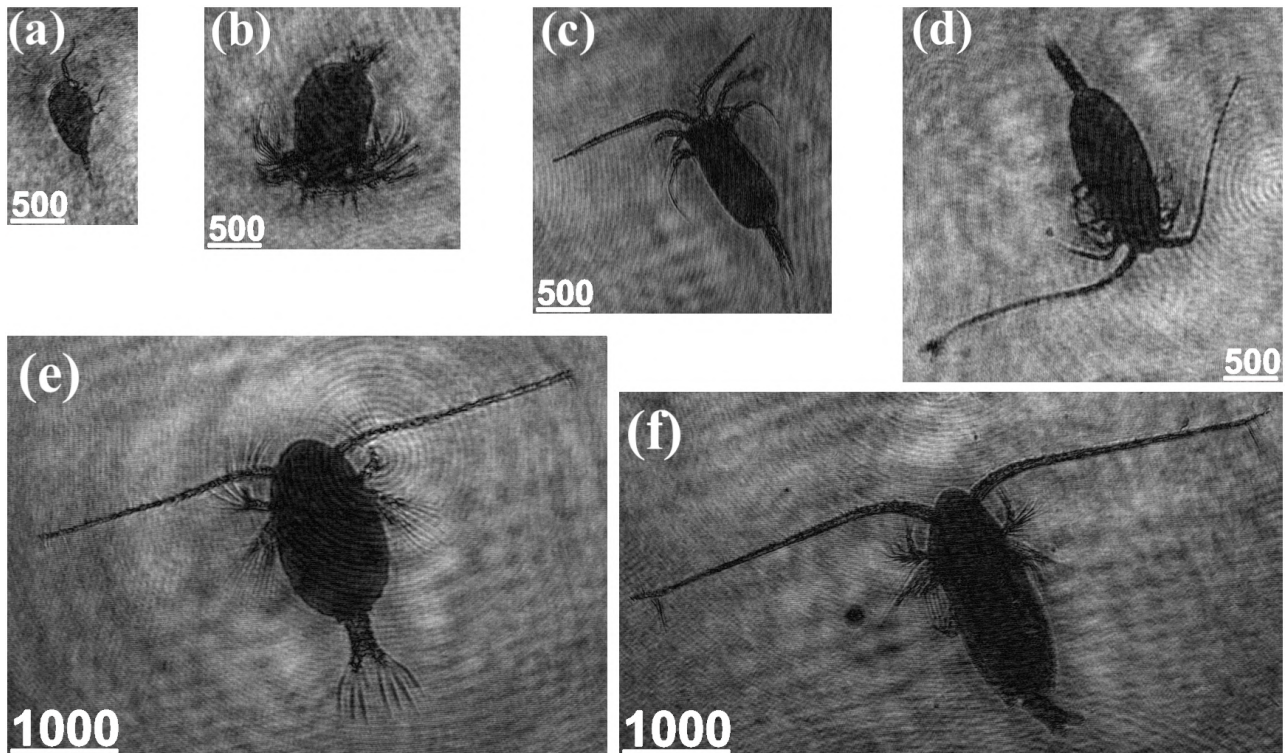
459
460 Fig. 16. Reconstructed holograms of six copepods of different size. (a) – Cop1; (b) – Cop2; (c) – Cop3;
461 (d) – Cop4; (e) – Cop5; (f) – Cop6. The unit of scale in the images is μm.
462
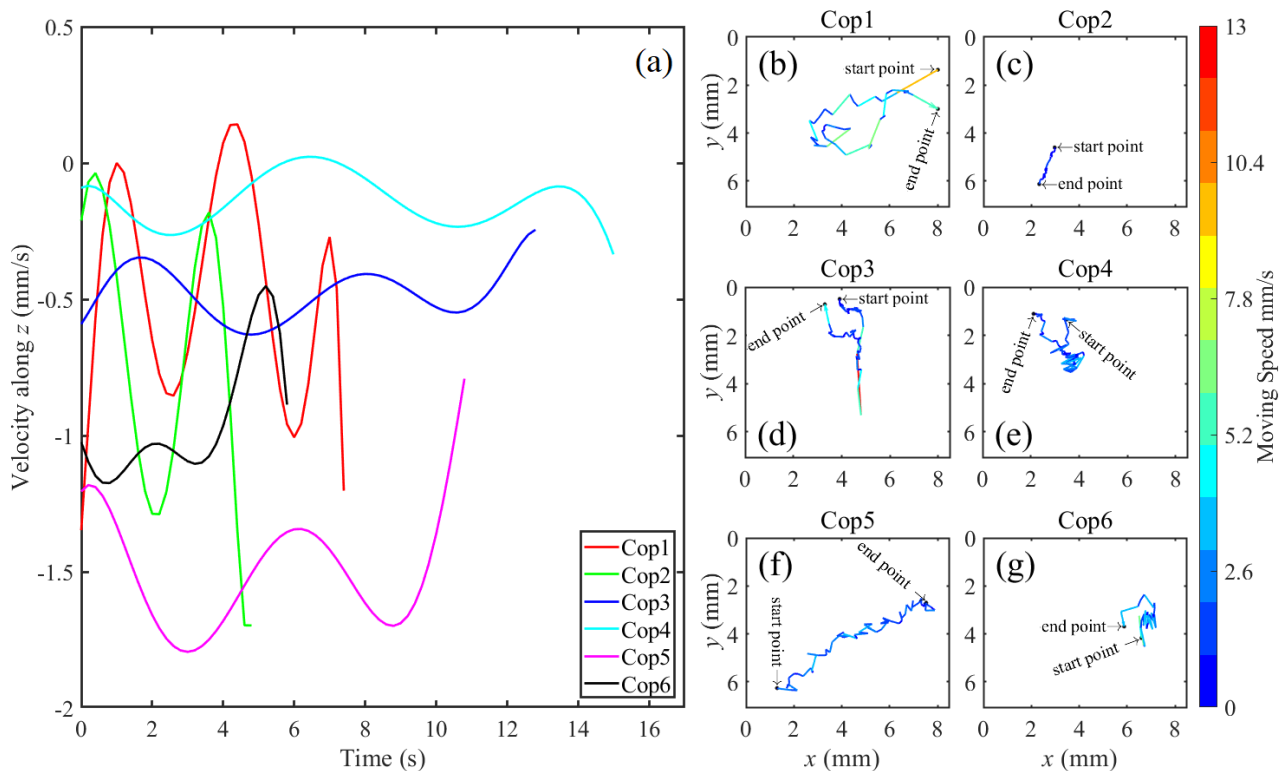
463
464 Fig. 17. Comparison of velocities along the z axis (a) and swimming trajectories with moving speeds
465 in the (x, y) plane of six copepods (b)-(g). The curves in (a) are generated using the method of
466 polynomial curve fitting.
467

468
469 TABLE 5. AVERAGE VELOCITIES ALONG THE Z AXIS AND MOVING SPEEDS IN THE (X, Y) PLANE OF SIX COPEPODS

Sample	Cop1	Cop2	Cop3	Cop4	Cop5	Cop6
Average Velocity along z (mm/s)	-0.48	-0.73	-0.48	-0.14	-1.49	-0.95
Average Moving Speed in x-y Plane	2.47	0.54	1.23	1.37	1.65	2.03

470

471 # 5 Conclusions

472 This work has demonstrated for the first time, multi-centimetre-extent vertical motion tracking of

473 sparsely distributed plankton and other particles at micrometre scale resolution using a novel, compact

474 and low-power, in-line holographic imaging system. The key findings of our experiments are:

475 • The combination of a CW laser with a short exposure (7 µs at shortest), low parasitic exposure

476 CMOS camera (pixel pitch – 3.45 µm × 3.45 µm) can obtain motion blur free holograms of organic

477 and inorganic particles travelling at up to 490 mm/s in theory. The maximum moving speed of

478 motion blur free tested in experiment is about 200 mm/s. This is sufficient to study the motion of

479 both active and inactive particles found in the ocean, from static or slow-moving sensing platforms.

480 With an in-line holographic measurement setup, we were able to record particles of a size down to

481 ~20 µm over a 20 cm long measurement channel with a 12 mL measurement volume. The

482 simplicity of this setup compared to systems that use pulsed lasers reduces the risk of optical

483 damage to components, increasing system reliability and offers potential size and power reductions.

484 This, combined with the ability to measure large volumes at micron-order resolution, could make

485 the setup more suitable for long-term monitoring of sparsely-distributed deep-sea particles than

486 conventional holographic imaging systems using pulsed lasers.

487 • The ability to track the vertical motion of a single particle over a several-centimetre range at a

488 micrometre-order resolution could allow differentiation between active, free-swimming organisms

489 such as live plankton, and inactive particles such as inorganic foraminifera shells. The ability to

490   distinguish particle type is significant when studying vertical transport of carbon and other

491   elements.

492 • The ability to measure behavioural patterns of active organisms also provides identical features

493   that can be used to facilitate the identification and classification of them at the species level.

494

Acknowledgements

500

References

502 [1] GOOS: The Global Ocean Observing System. https://www.goosocean.org (accessed Apr. 29,

503 2020).

504 [2] F. Lombard, E. Boss, A. Waite, et al, "Globally consistent quantitative observations of planktonic

505 ecosystems," *Front. Mar. Sci.*, vol. 6:196, Apr. 2019.

506 [3] A. Gupta, A. Roy, A. Saha, and S. S. Ray, "Flocking of active particles in a turbulent flow," *Phys.

507 Rev. Fluids*, vol. 5, 052601(R), May 2020.

508 [4] E. Sodré and R. Bozelli, "How planktonic microcrustaceans respond to environment and affect

509 ecosystem: a functional trait perspective," *Int. Aquat. Res.*, vol. 11, pp. 207–223, Jul. 2019.

510 [5] D. Lindsay, A. Yamaguchi, M. Grossmann, et al, "Vertical profiles of marine particulates: a step

511 towards global scale comparisons using an Autonomous Visual Plankton Recorder," *Bull. Plankton

512 Soc. Japan*, vol. 61, no. 1, pp. 72–81, 2014.

513   [6] A. Jamieson, L. Brooks, W. Reid, S. Piertney, B. Narayanaswamy, and T. Linley, "Microplastics

514   and synthetic particles ingested by deep-sea amphipods in six of the deepest marine ecosystems on

515   Earth," *R. Soc. Open Sci.*, vol. 6:180667, Feb. 2019.

516   [7] S. Giering, E. Cavan, S. Basedow, et al, "Sinking organic particles in the ocean—flux estimates

517   from in situ optical devices," *Front. Mar. Sci.*, vol. 6:834, Feb. 2020.

518   [8] E. Malkiel, J. Sheng, J. Katz, and J. Strickler, "The three-dimensional flow field generated by a

519   feeding calanoid copepod measured using digital holography," *J. Exp. Biol.*, vol. 206, pp. 3657–3666,

520   Jul. 2003.

521   [9] B. Gemmella, J. Sheng, and E. Buskeya, "Compensatory escape mechanism at low Reynolds

522   number," *PNAS*, vol. 110, no. 12, pp. 4661–4666, Mar. 2013.

523   [10] M. Sohn, S. Lim, K. Seo, and S. LEE, "Effect of ambient medium viscosity on the motility and

524   flagella motion of *Prorocentrum minimum* (Dinophyceae)," *J. Plankton Res.*, vol. 35, no. 6, pp. 1294–

525   1304, Jul. 2013.

526   [11] A. Mullen1, T. Treibitz, P. Roberts, E. Kelly, R. Horwitz, J. Smith, and J. Jaffe, "Underwater

527   microscopy for in situ studies of benthic ecosystems," *Nat. Commun.*, vol. 7: 12093, Jul. 2016.

528   [12] J. Song, H. Bib, Z. Cai, X. Cheng, Y. He, M. C. Benfield, and C. Fan, "Early warning of Noctiluca

529   scintillans blooms using in-situ plankton imaging system: An example from Dapeng Bay, P.R. China,"

530   *Ecol. Indic.*, vol 112: 106123, Jan. 2020.

531   [13] M. Lunven, J. Landeira, M. Lehaître, R. Siano, C. Podeur, and M. Madeleine, "In situ video and

532   fluorescence analysis (VFA) of marine particles: applications to phytoplankton ecological studies,"

533   *Limnol. Oceanogr.: Methods*, vol. 10, pp. 807–823, Oct. 2012.

534   [14] T. Colomb, N. Pavillon, J. Kühn, E. Cuche, C. Depeursinge, and Y. Emery, "Extended depth-of-

535   focus by digital holographic microscopy," *Opt. Lett.*, vol. 35, no. 11, pp. 1840–1842, Jun. 2010.

[15] U. Schnars, C. Falldorf, J. Watson, and W. Jüptner, "Digital Holographic Particle Sizing and Microscopy," in *Digital Holography and Wavefront Sensing*, 2th ed. Berlin, Heidelberg, Germany: Springer, 2015, ch. 5, sec. 2, pp. 96–104.

[16] J. Garcia-Sucerquia, W. Xu, S. Jericho, P. Klages, M. Jericho, and H. Kreuzer, "Digital in-line holographic microscopy," *Appl. Opt.*, vol. 45, no. 5, pp. 836–850, Feb. 2006.

[17] J. Flewellen, I. Zaid, and R. Berry, "A multi-mode digital holographic microscope," *Rev. Sci. Instrum.*, vol. 90: 023705, Feb. 2019.

[18] D. Pfitsch, E. Malkiel, Y. Ronzhes, S. King, J. Sheng, and J. Katz, "Development of a free-drifting submersible digital holographic imaging system," in MTS/IEEE Oceans 2005, Washington, DC, USA, Sep. 2005.

[19] S. Talapatra, J. Sullivan, J. Katz, M. Twardowski, H. Czerski, P. Donaghay, J. Hong, R. Jan, M. McFarland, A. Nayak, and C. Zhang, "Application of in-situ digital holography in the study of particles, organisms and bubbles within their natural environment," in Proc. SPIE 8372, Ocean Sensing and Monitoring IV, 837205, Baltimore, Maryland, USA, Jun. 2012.

[20] H. Sun and D. Hendry and M. Player, and John Watson, "In situ underwater electronic holographic camera for studies of plankton," *IEEE J. Ocean. Eng.*, vol. 32, no. 2, pp. 373–382, Apr. 2007.

[21] 4Deep: HoloSea. http://4-deep.com/products/submersible-microscope/ (accessed Apr. 29, 2020).

[22] SEQUOIA: LISST-Holo2. https://www.sequoiasci.com/product/lisst-holo/ (accessed Apr. 29, 2020).

[23] F. Göltenboth, S. Schoppe, and P. Widmann, "Open Ocean," in *Tropical Ecology of Southeast Asia*, F. Goltenboth, K. Timotius, P. Milan, and J. Margraf, Ed. Amsterdam, The Netherlands, Elsevier, 2006, ch. 2, sec. 5, pp. 71–84.

[24] J. Mateos-Perez, R. Redondo, R. Nava, et al, "Comparative evaluation of autofocus algorithms for a real-time system for automatic detection of *Mycobacterium tuberculosis*," *Cytom. Part A*, vol. 81, no. 3, pp. 213–221, Mar. 2012.

561   [25] T. Yokoyama, M. Tsutsui, M. Suzuki, Y. Nishi, I. Mizuno, and A. Lahav, "Development of low

562   parasitic light sensitivity and low dark current 2.8 μm global shutter pixel," *Sensors*, vol. 18, no. 2:

563   349, Feb. 2018.

564   [26] A. Visser, "Motility of zooplankton: fitness, foraging and predation," *J. Plankton Res.*, vol. 29,

565   no. 5, pp. 447–461, May 2007.

566   [27] C. Borg, E. Bruno, and T. Kiørboe, "The kinematics of swimming and relocation jumps in

567   copepod nauplii," *PLoS ONE*, vol. 7, no. 10: e47486, Oct. 2012.

568   [28] M. McManus and C. Woodson, "Plankton distribution and ocean dispersal," *J. Exp. Biol.*, vol.

569   215, pp. 1008–1016, Feb. 2012.

570   [29] D. Stearns and R. Forward, Jr., "Copepod photobehavior in a simulated natural light environment

571   and its relation to nocturnal vertical migration," *Mar. Biol.*, vol. 82, pp. 91–100, Aug. 1984.

572   [30] L. Lain and S. Bernard, "The fundamental contribution of phytoplankton spectral scattering to

573   ocean colour: implications for satellite detection of phytoplankton community structure," *Appl. Sci.*,

574   vol. 8, no. 12:2681, Dec. 2018.

575   [31] G. Graham and W. Nimmo-Smith, "The application of holography to the analysis of size and

576   settling velocity of suspended cohesive sediments," *Limnol. Oceanogr.: Methods*, vol. 8, pp. 1–15, Jan.

577   2010.

578   [32] A. Bochdansky, M. Jericho, and G. Herndl, "Development and deployment of a point-source

579   digital inline holographic microscope for the study of plankton and particles to a depth of 6000 m,"

580   *Limnol. Oceanogr.: Methods*, vol. 11, pp. 28–40, Jan. 2013.

581   [33] T. Latychevskaia and H. Fink, "Practical algorithms for simulation and reconstruction of digital

582   in-line holograms," *Appl. Opt.*, vol. 54, no. 9, pp. 2424–2434, Mar. 2015.

583   [34] J. Mateos-Perez, R. Redondo, R. Nava, et al, "Comparative evaluation of autofocus algorithms

584   for a real-time system for automatic detection of *Mycobacterium tuberculosis*," *Cytom. Part A*, vol.

585   81, no. 3, pp. 213–221, Mar. 2012.

586   [35] P. Dollar and C. Zitnick, "Structured forests for fast edge detection," in IEEE Int. Conf. Comput.

587   Vis., pp. 3–8, Sydney, NSW, Australia, Dec. 2013.

588   [36] K. D. Mielenz, "On the Diffraction Limit for Lensless Imaging," *J. Res. Natl. Inst. Stand. Technol.*,

589   pp. 479–485, vol. 104, no. 479, 1999.

590   [37] J. van Rooij and J. Kalkman "Axial-resolution in depth from focus digital holography," in Proc.

591   SPIE 10335, Digital Optical Technologies 2017, Munich, Germany, Jun. 2017.

592   [38] S. Dai and Y. Wu, "Motion from blur," in IEEE Conf. Comput. Vis. Pattern Recogn., Anchorage,

593   USA, Jun. 2008.

594   [39] B. Pueo, "High speed cameras for motion analysis in sports science," *J. Hum. Sport Exerc.*, vol.

595   11(1), pp. 53–73, 2016.

596   [40] Deep Tow (JAMSTEC, Japan).

597   https://www.jamstec.go.jp/e/about/equipment/ships/deeptow.html (accessed Apr. 20, 2020).